Reversible Silicon Anodes with Long Cycles by Multifunctional Volumetric Buffer Layers

Tiansheng Mu, Shuaifeng Lou, Nathaniel Graham Holmes, Changhong Wang, Mengxue He, Baicheng Shen, Xiaoting Lin, Pengjian Zuo,* Yulin Ma, Ruying Li, Chunyu Du, Jiajun Wang, Geping Yin,* and Xueliang Sun*

Read Online

ACCESS | Metrics & More | Article Recommendations | Supporting Information

ABSTRACT: Establishing a stable, stress-relieving configuration is imperative to achieve a reversible silicon anode for high energy density lithium-ion batteries. Herein, we propose a silicon composite anode (denoted as T-Si@C), which integrates free space and mixed carbon shells doped with rigid TiO_2/Ti_5Si_3 nanoparticles. In this configuration, the free space accommodates the silicon volume fluctuation during battery operation. The carbon shells with embedded TiO_2/Ti_5Si_3 nanoparticles maintain the structural stability of the anode while accelerating the lithium-ion diffusion kinetics and mitigating interfacial side reactions. Based on these advantages, T-Si@C anodes demonstrate an outstanding lithium storage performance with impressive long-term cycling reversibility and good rate capability. Additionally, T-Si@C//LiFePO$_4$ full cells show superior electrochemical reversibility. This work highlights the importance of rational structural manipulation of silicon anodes and affords fresh insights into achieving advanced silicon anodes with long life.

KEYWORDS: *free space, multifunctional buffer, ion-electron transport, mechanical stability, silicon anodes*
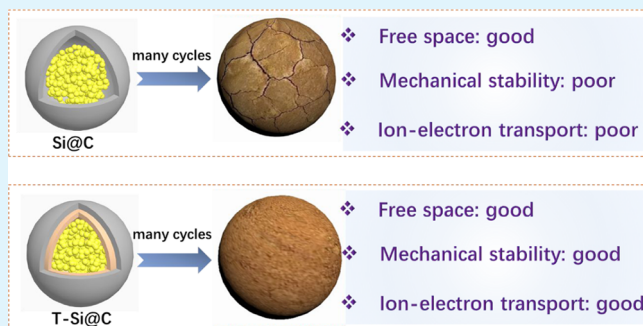
1. INTRODUCTION

Growing demand for smart grids and electric vehicles has spurred intense research into rechargeable batteries with high energy density and long life span. The state-of-the-art commercial graphite-based rechargeable batteries based on the intercalation mechanism are approaching a theoretical capacity limit.[1,2] Therefore, electrode materials with novel lithium storage mechanisms are required to achieve higher energy density.[3,4] Silicon anodes, functioning via an alloying/dealloying mechanism, are generally considered the most promising next-generation anode material due to their astonishing theoretical capacity (4200 mA h g^{-1}) and cost-effectiveness.[5,6] Despite these advantages, commercial adoption of silicon anodes has been hindered by poor electrochemical reversibility due to expansion/contraction and unstable interfacial chemistry.[7] Moreover, the drastic volume change fractures the fragile solid electrolyte interface (SEI), leading to poor Coulombic efficiencies.[8,9] Alleviating the volumetric fluctuation and maintaining the interfacial chemical stability are therefore essential and necessary to realizing a stable silicon anode.

To address the problems of silicon anodes, tremendous efforts have been devoted to enhancing the structural and chemical stability. Dimensional design (nanowires,[10] nanotubes,[1,11] quantum dots[12,13]), hierarchical construction (pomegranate-like structure,[10] granadilla-like framework[14]), optimization of electrolytes (lithium salts,[15] solvents,[16] and additives[17]), and advanced binders[18] have been proposed to increase the cyclability of silicon anodes. Some surface-engineered artificial coatings have greatly prolonged the cycle life of silicon anodes.[19] However, batteries still fail after hundreds of cycles due to inevitable coating breakage. Besides, the lithium-ion diffusion kinetics of coatings also greatly affect the performance of silicon anodes. With artificial coatings, good ionic conductivity and better wettability with electrolytes accelerate the electrochemical kinetics.[20] It is now recognized that both good mechanical stability and fast electron-ion kinetics are indispensable to realize long-life cycling silicon anodes.

It is often difficult to achieve good structural stability when combining individual functional materials with silicon anodes due to insufficient mechanical strength. Some recently

developed oxide coatings (e.g., TiO_2, Mn_3O_4) have prolonged the service life of silicon anodes.[20,21] Yet, mechanical brittleness and sluggish electron transport remain challenges, which inhibit their widespread use.[22−25] Some polymer coatings with excellent flexibility have been considered as an effective strategy to improve the electronic conductivity of electrode materials. For example, Yi et al. reported for the first time that polypyrrole could be used as a conducting layer to improve the electronic conductivity and cycle performance of the $Li_5Cr_7Ti_6O_{25}$ composite.[26] However, polymer coatings usually cause sluggish ion transport.[27] Introducing free space into silicon composites can improve the ability of silicon anodes to adapt to volume changes, which is a generally accepted view.[28,29] However, relying on free space alone to act as a buffer for stresses, which develop within the material, is inadequate for long-term reversibility of silicon anodes. It is therefore expected that multifunctional components or synergistic structures integrated into hybrid silicon architectures will be a key enabler of next-generation silicon anodes.

We propose a silicon composite anode (denoted as T-Si@C) with stress relief achieved by integrating free space and mixed ion/electron-conducting shells composed of carbon and TiO_2/Ti_5Si_3 particles. In this configuration, the free space and the heterogeneous shells synergistically provide an effective mechanical buffer, fast ion-electron transport kinetics, and favorable interfacial stability. As a consequence, T-Si@C anodes exhibit superior electrochemical performance with improved Coulombic efficiencies, long-term cycling reversibility, and enhanced rate capability. Besides, the full cells paired with $LiFePO_4$ cathodes reach an energy density of 400 Wh kg^{-1} and display good cycling stability with a capacity retention of 87% after 80 cycles.

2. RESULTS AND DISCUSSION

A schematic diagram of the T-Si@C anode preparation process is shown in Figure 1. SiO_2 spheres were first modified with
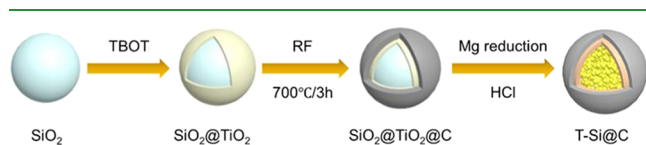
**Figure 1.** Schematic diagram of the preparation process of the T-Si@C anode.

hydroxyl propyl cellulose (HPC), whereby with the numerous hydroxyl groups stick to the silica surface.[30] Titanium butoxide (as the TiO_2 precursor) was then deposited on the silica sphere surface. Anatase TiO_2 was then obtained by high-temperature sintering in air, removing the HPC in the process. The resorcinol−formaldehyde (RF) resin was then polymerized in situ on the TiO_2@SiO_2 spheres, and a uniform carbon shell was obtained by carbonization. A magnesiothermic reduction reaction was performed in a sealed high-temperature high-pressure reactor as shown in Figure S1, and a series of reactions occurred per the reaction equations given below. In this process, SiO_2 was reduced to crystalline silicon particles. Simultaneously, TiO_2 was partly converted to titanium (eqs 1 and 2).[31,32] Titanium and silicon partly reacted to generate titanium silicide (Ti_5Si_3) (eq 3).[33,34] Finally, T-Si@C anodes were obtained after acid washing.

$$SiO_2 + Mg \rightarrow Si + MgO \tag{1}$$

$$TiO_2 + Mg \rightarrow Ti + MgO \tag{2}$$

$$5Ti + 3Si \rightarrow Ti_5Si_3 \tag{3}$$
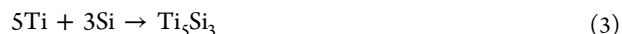
X-ray diffraction (XRD) was performed to determine the crystal structure and composition. The SiO$_2$@C pattern shows a broad peak at ~23° as shown in Figure S2, indicating an amorphous structure of SiO_2 and carbon.[13] For SiO_2@TiO_2@C, some obvious diffraction peaks can be observed in Figure S3, corresponding to anatase TiO_2 (JCPDS no. 21-1272).[23] After the magnesiothermic reduction reaction, the characteristic peaks of crystalline silicon were observed in the Si@C and T-Si@C XRD spectra as shown in Figure 2a. The well-defined peaks at 28.5, 47.4, 56.2, 69.3, and 76.4° are assigned to the (111), (220), (311), (400), and (331) planes of crystallized silicon (JCPDS no. 27-1402), respectively.[35,36] Notably, the two peaks of anatase TiO_2 and Ti_5Si_3 can be observed in the spectra of T-Si@C, as we described in the reaction equations above.[37] Specifically, the diffraction peak at 25.3° can be assigned to the (101) plane diffraction of anatase TiO_2.[38] The diffraction peak at 41.1° can be attributed to the (211) plane diffraction of Ti_5Si_3.[34] The rigid TiO_2/Ti_5Si_3 particles not only promote fast ion-electron diffusion kinetics but also mechanically strengthen the hybrid configuration. Meanwhile, the carbon shell is electrically conductive. This integrated configuration is essential for realizing a stable silicon anode with a long life span. Further, X-ray absorption spectroscopy (XAS) was also performed. It is noteworthy that the titanium optoelectronic signals are hardly observable by X-ray photoelectron spectroscopy (XPS) because the thickness of the carbon shell is beyond the detection range (~10 nm). The Ti L-edge signal can be seen in Figure 2b, confirming the presence of titanium-based compounds.

A thermogravimetric (TG) test was carried out to assess the carbon content and estimate the degree of magnesiothermic reduction. As shown in Figure S4, the carbon content of SiO_2@C and SiO_2@TiO_2@C is 20.1 and 19.8%, respectively. For Si@C and T-Si@C, the carbon content is 28.5 and 30.5% as shown in Figure 2c, respectively. The theoretical carbon content for Si@C, calculated according to the ideal magnesiothermic reduction reaction, is 35%. Yet, complex reaction processes including gas−solid reactions and solid−solid diffusion reactions produce a variety of reaction products in the actual magnesiothermic reaction process.[39] Side reactions and the presence of unreacted silica always occur, causing the carbon content to deviate from the theoretical value. Nevertheless, a good conversion rate was achieved due to the use of homogeneous mixed precursors and a closed, high-pressure stainless-steel reaction environment. It is remarkable that the content of the Ti_5Si_3/TiO_2 compounds cannot be determined for T-Si@C. There is only a small difference in the carbon content of Si@C and T-Si@C, probably due to the small amount of the Ti_5Si_3/TiO_2 compound.

Further, the microstructure and morphology were characterized by scanning electron microscopy (SEM) and transmission electron microscopy (TEM). The diameter of the SiO_2 spheres with a smooth surface is uniformly distributed around 300 nm as shown in Figure S5. After carbon coating, SiO_2@C remains spherical as shown in Figure S6. Similarly, the spherical morphologies of SiO_2@TiO_2 and SiO_2@TiO_2@C are maintained as shown in Figure S7. Si@C and T-Si@C exhibit a typical yolk−shell structure, which can be observed in the individual cracked samples shown in Figure 2d,h. Four
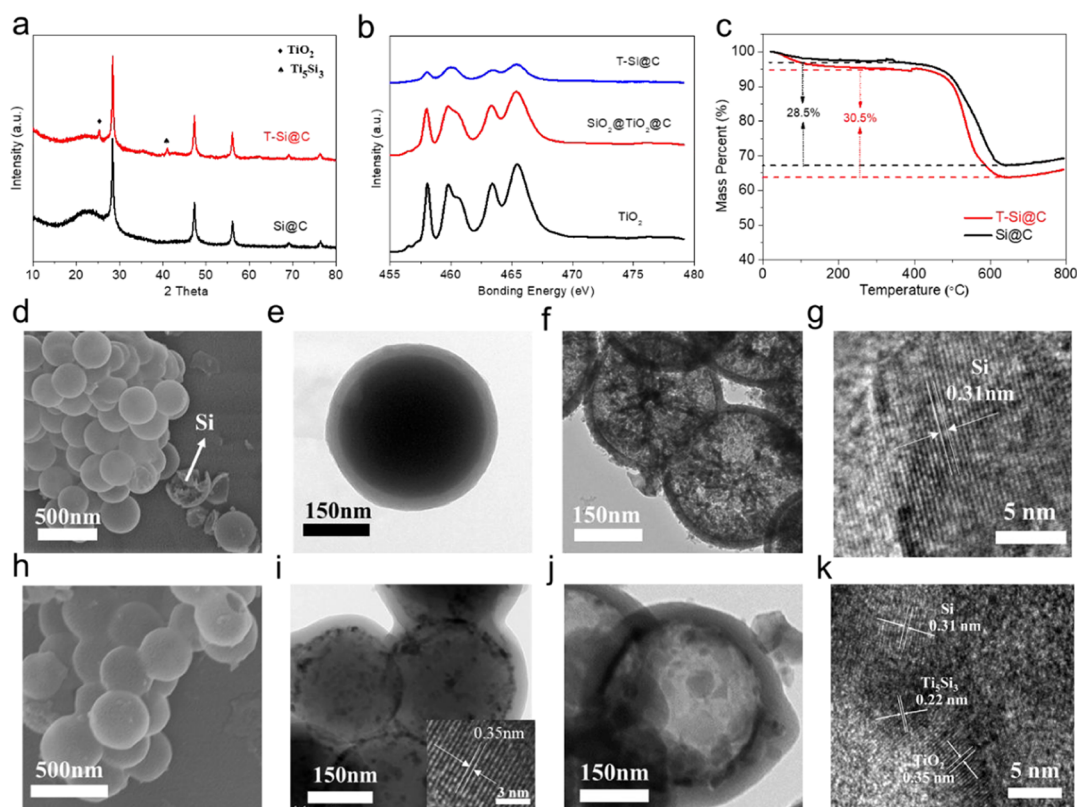
Figure 2. (a) XRD patterns of Si@C and T-Si@C; (b) Ti L-edge X-ray absorption spectra; (c) TG curves of Si@C and T-Si@C in air; (d) SEM image of Si@C; (e) TEM image of SiO$_2$@C; (f) TEM image of Si@C; (g) HRTEM image of Si@C; (h) SEM image of T-Si@C; (i) TEM image of SiO$_2$@TiO$_2$@C; (j) TEM image of T-Si@C; and (k) HRTEM image of T-Si@C.

elements (Si, Ti, C, O) can be seen on the EDS line scan of T-Si@C in Figure S8. For SiO$_2$@C and SiO$_2$@TiO$_2$@C, the thicknesses of the carbon layers are uniformly distributed around 30 nm (Figure 2e,i). In contrast to SiO$_2$@C, there is a distinct layer of TiO$_2$ particles between the carbon layer and the SiO$_2$ spheres in SiO$_2$@TiO$_2$@C. The TiO$_2$ lattice fringes are shown in the inset, and the interplanar spacing of 0.35 nm corresponds to the (101) plane of anatase TiO$_2$.[23] A yolk–shell construction is observed for Si@C and T-Si@C in Figure 2f,j, confirming the SEM results. In contrast, T-Si@C has a TiO$_2$/Ti$_5$Si$_3$ layer inside the carbon shell. Note that this TiO$_2$/Ti$_5$Si$_3$ layer presents as inlaid particles in the heterogeneous shell, evident by the detailed examination of Figure S9. Titanium-based compound signals were also detected by EDS at the points shown in Figure S10. The embedded TiO$_2$/Ti$_5$Si$_3$ particles in the hybrid shell are more conducive to the ion-electron transport compared to a uniform layer. The silicon lattice fringe is observed in Figure 2g,k, and an interplanar spacing of 0.31 nm belonging to the (111) plane of silicon shows successful reduction of SiO$_2$.[40] Meanwhile, lattice fringes of TiO$_2$ and Ti$_5$Si$_3$ are shown in Figure 2k. The interplanar spacings of 0.35 and 0.22 nm correspond to the (101) plane of anatase TiO$_2$ and the (211) plane of Ti$_5$Si$_3$.[34] Herein, TiO$_2$ and Ti$_5$Si$_3$ both have higher mechanical strength relative to carbon materials. Particularly, Ti$_5$Si$_3$ possesses very high hardness, which has a great advantage for buffering the volume strain/stress of silicon.[33,37] Meanwhile, TiO$_2$ has good ion transport capability, and Ti$_5$Si$_3$ has a high electrical conductivity.[34,41] Therefore, the TiO$_2$/Ti$_5$Si$_3$ layer is beneficial to accelerate the ion-electron transport dynamics. This designed configuration integrates free space and a heteroge-

neous shell structure to yield a T-Si@C anode with exceptional cycle reversibility.

The electrochemical lithium storage performance was investigated for T-Si@C and Si@C and is shown in Figure 3. Commercial silicon nanoparticles (nano-Si) were used as the control sample. The initial three charge/discharge curves of T-Si@C at 200 mA g^{-1} are shown in Figure 3a. The initial discharge/charge specific capacities are 2238.0 and 1300.0 mA h g^{-1}, respectively. The corresponding initial Coulombic efficiency (CE) is 58.0%. The large irreversible capacity is due to the formation of the SEI and irreversible reactions between lithium ions and oxygenated functional groups on the carbon surfaces.[42,43] Additionally, residual unreduced SiO$_2$ may also consume lithium ions.[44] This low CE can be improved by the prelithiation method in future work.[45] At present, the prelithiation method is one of the most effective methods to improve the first CE of silicon-based anodes. For example, stabilized lithium metal powders (SLMP) or lithium foil can be used to realize the prelithiation.[46,47] As expected, the Si@C anodes display a similarly low initial CE of 56.5% (Figure S11). These first Coulombic efficiencies are lower than those of nano-Si anodes (74.3%) as shown in Figure S12. Cyclic voltammetry (CV) curves of T-Si@C demonstrate the typical electrochemical alloy/de-alloy behavior of crystalline silicon (Figure 3b).[35] Specifically, the sharp peak at ~0.01 V in the first lithiation process corresponds to the conversion reaction from crystalline silicon to an amorphous Li$_x$Si alloy. The peak at ~0.2 V detected from the second cycle represents the alloying reaction between lithium and amorphous silicon. During the following delithiation scan, the peaks at ~0.36 and ~0.52 V are attributed to the dealloying reactions from Li$_x$Si to
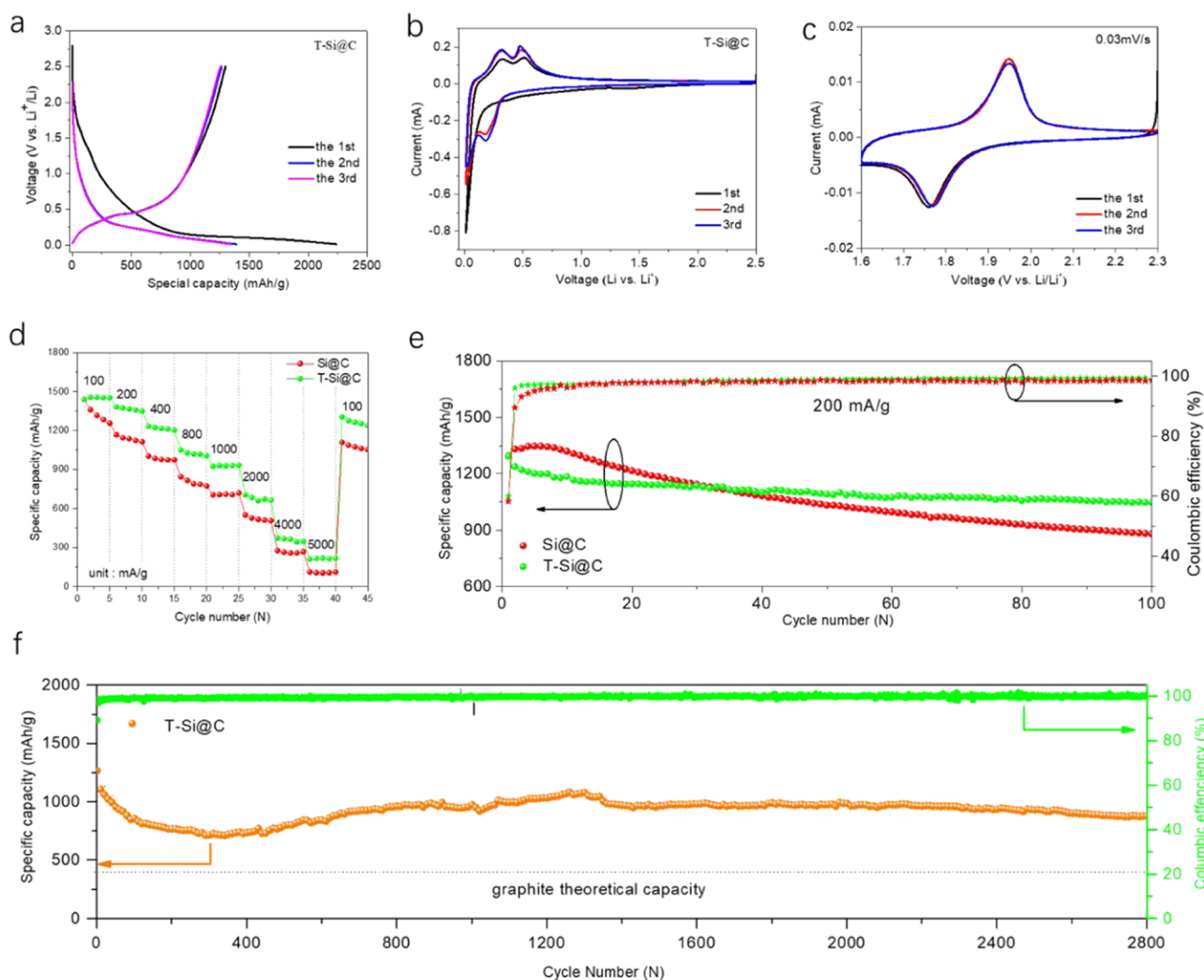
Figure 3. (a) Charge/discharge curves of T-Si@C at 200 mA g^{-1}; (b) CV curves of T-Si@C at 0.1 mV s^{-1}; (c) local CV curves of T-Si@C anodes at 0.03 mV s^{-1}; (d) rate performance; (e) cycling stability at 200 mA g^{-1}; (f) long-term cycling performance of T-Si@C at 500 mA g^{-1} (the initial three cycles at 200 mA g^{-1}).

amorphous silicon. To more clearly observe the TiO$_2$ redox peak, the CV scan rate was lowered to 0.03 mV s^{-1} from 1.6 to 2.3 V. The peaks at ∼1.75 and 1.95 V correspond to the lithiation/delithiation of anatase TiO$_2$ (Figure 3c).[48] Notably, the CV redox peaks corresponding to Ti$_5$Si$_3$ were not observed, which may be related to the low electrochemical activity or low content of Ti$_5$Si$_3$. In comparison, the CV curves of Si@C exhibit similar features with the exception of the missing TiO$_2$ redox peak as shown in Figure S13.

The rate capability was investigated as shown in Figure 3d. The T-Si@C anode displays better rate performance than Si@C under corresponding current densities due to the better mechanical stability and ion-electron transfer. Compared to the rate retention of nano-Si anodes shown in Figure S14, both Si@C and T-Si@C anodes demonstrate a significant improvement, indicating the ability of the free space to buffer volume fluctuations. The cyclability at 200 mA g^{-1} was tested as shown in Figure 3e. The T-Si@C anodes show higher capacity retention (81%) compared to the Si@C anodes (67%). A reversible capacity of 1047 mA g^{-1} is maintained after 100 cycles. The T-Si@C anodes also exhibit higher Coulombic efficiencies than the Si@C anodes, indicating more stable interfacial chemistry with T-Si@C anodes. The reason for this

is that the carbon shells in the Si@C anodes become damaged, and the SEI is repeatedly repaired during cycling. With the T-Si@C anodes, a robust heterogeneous shell increases the structural stability and allows for outstanding reversible electrochemical cycling. In comparison, the nano-Si anodes display the least cycle stability (Figure S15) and retain only 15% capacity. Finally, the ultra-long cycling performance of the T-Si@C anodes was tested at 500 mA g^{-1}. The activation current of the initial three cycles is 200 mA g^{-1}. The electrochemical cycling data and corresponding Columbic efficiencies are shown in Figure 3f. A reversible capacity of 876 mA h g^{-1} was retained after 2800 cycles, more than twice the theoretical capacity of the commercial graphite. We noticed that the specific capacity curve presents some fluctuations with preliminary decline and subsequent recovery during cycling. This is most likely related to the sustained activation of some active silicon during cycling or temperature fluctuations. Similar phenomena have appeared in previous reports.[13,49−51] The T-Si@C anode shows outstanding long-term cycling stability and rate capability benefiting from multiple buffering mechanisms including the free space and the robust heterogeneous shells composed of carbon and rigid TiO$_2$/Ti$_5$Si$_3$ particles.
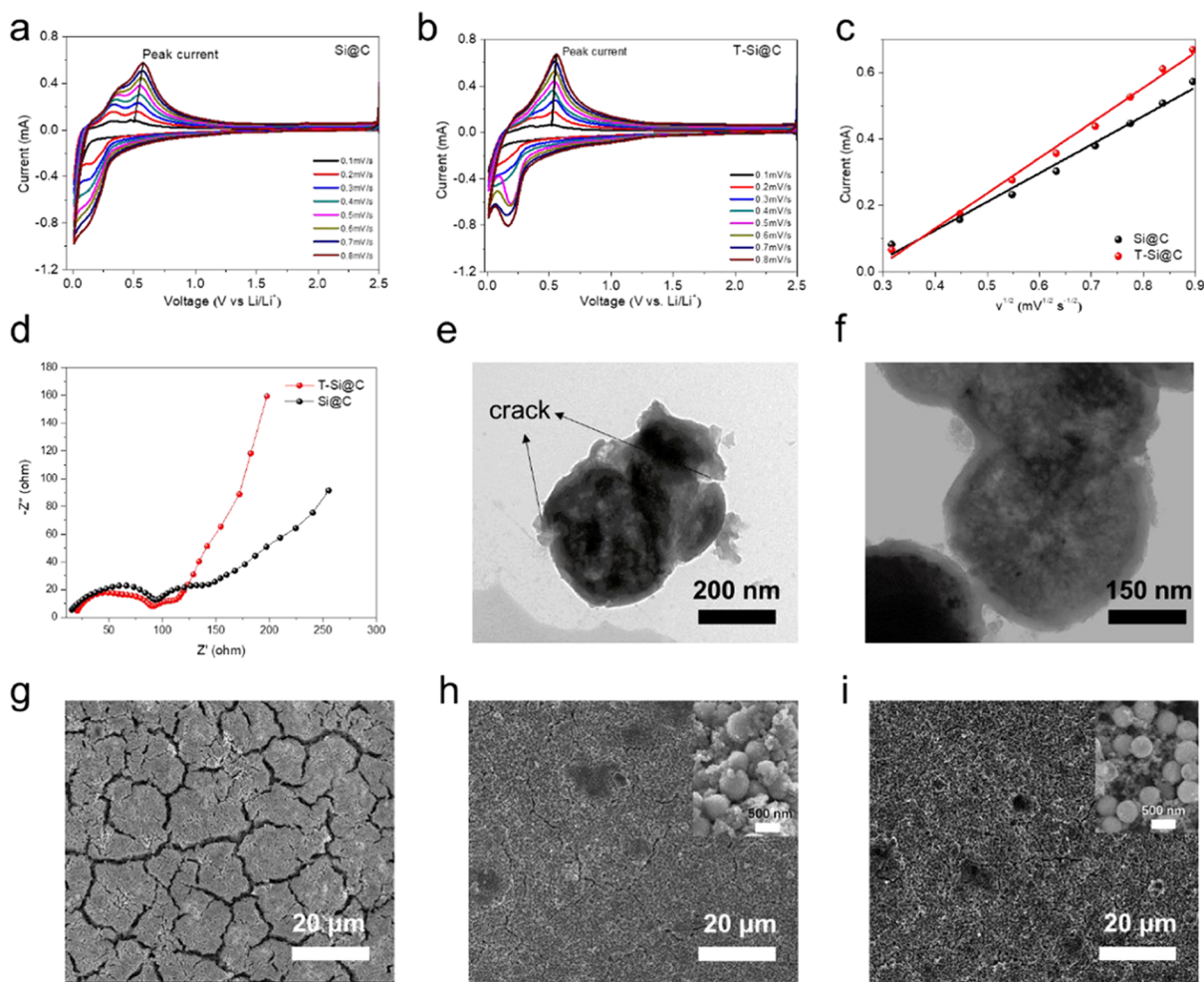
Figure 4. CV curves at various scan rates: (a) Si@C and (b) T-Si@C; (c) linear relationship between the cathodic peak current (I_p) and the square root of the scan rate ($\nu^{1/2}$) for Si@C and T-Si@C; (d) the EIS spectra of Si@C and T-Si@C after 100 cycles. TEM images after 100 cycles: (e) Si@C and (f) T-Si@C; SEM images after 100 cycles: (g) nano-Si electrode, (h) Si@C electrode, and (i) T-Si@C electrode.

To evaluate the lithium-ion diffusion kinetics, CV curves of the Si@C and T-Si@C anodes were recorded at different scan rates from 0.1 to 0.8 mV s^{-1}. As shown in Figure 4a,b, the intensity of the cathodic and anodic peaks gradually increases with increasing scan rate.[42] The apparent lithium-ion diffusion coefficient in the electrodes can be calculated by the Randles–Sevcik equation

$$I_p = 0.4463\, n^{2/3} F^{3/2} R^{-1/2} T^{-1/2} A\, D^{1/2} C \nu^{1/2} \tag{4}$$

In eq 4, I_p is the peak current, n is the charge transfer number, F is the Faraday constant, R is the gas constant, T is the absolute temperature, D is the diffusion coefficient of lithium ions, A is the electrode surface area, C is the concentration, and ν is the scan rate.[12] As the preparation processes for Si@C and T-Si@C anodes are the same, eq 4 can be simplified as follows

$$I_p = S D^{1/2} \nu^{1/2} \tag{5}$$

In eq 5, S is a battery-related constant, so the lithium-ion diffusion coefficient can be compared by linear relationship between the cathodic peak current (I_p) and the square root of the scan rate ($\nu^{1/2}$). The larger the slope, the faster the diffusion. The peaks at ~0.5 V in the positive scan were selected as the research object due to their ease of observation. In Figure 4c, the T-Si@C anode presents a larger slope than

that of the Si@C anode. The T-Si@C anode shows faster lithium-ion diffusion kinetics, indicating that the rigid TiO$_2$/Ti$_5$Si$_3$ nanoparticles on the carbon shells accelerate the lithium-ion diffusion dynamics.

Electrochemical impedance spectra (EIS) were measured after 100 cycles as illustrated in Figure 4d. The impedance spectrum displays two semicircles in the high frequency region and a straight line in the low frequency region, representing SEI resistance (R_{SEI}), charge transfer resistance (R_{ct}), and lithium-ion diffusion, respectively.[52] The straight line slope reflects the apparent lithium-ion diffusion in the electrode. Specifically, the larger the slope, the faster the lithium-ion diffusion.[53] It can be observed that the T-Si@C anodes present faster lithium-ion diffusion than the Si@C anodes, which is consistent with the results shown in Figure 4c. Accelerated lithium-ion diffusion is one key factor required for improving the rate capability of T-Si@C anodes. The T-Si@C anodes also display a smaller charge transfer resistance than the Si@C anodes. As a contrast sample, the EIS spectra of the nano-Si electrode after 100 cycles was also tested as shown in Figure S16. It can be seen clearly that the nano-Si electrode shows the larger R_{SEI} resistance and R_{ct} resistance relative to the T-Si@C electrode and Si@C electrode after 100 cycles. Besides, the straight line slope of the nano-Si electrode is also lower than
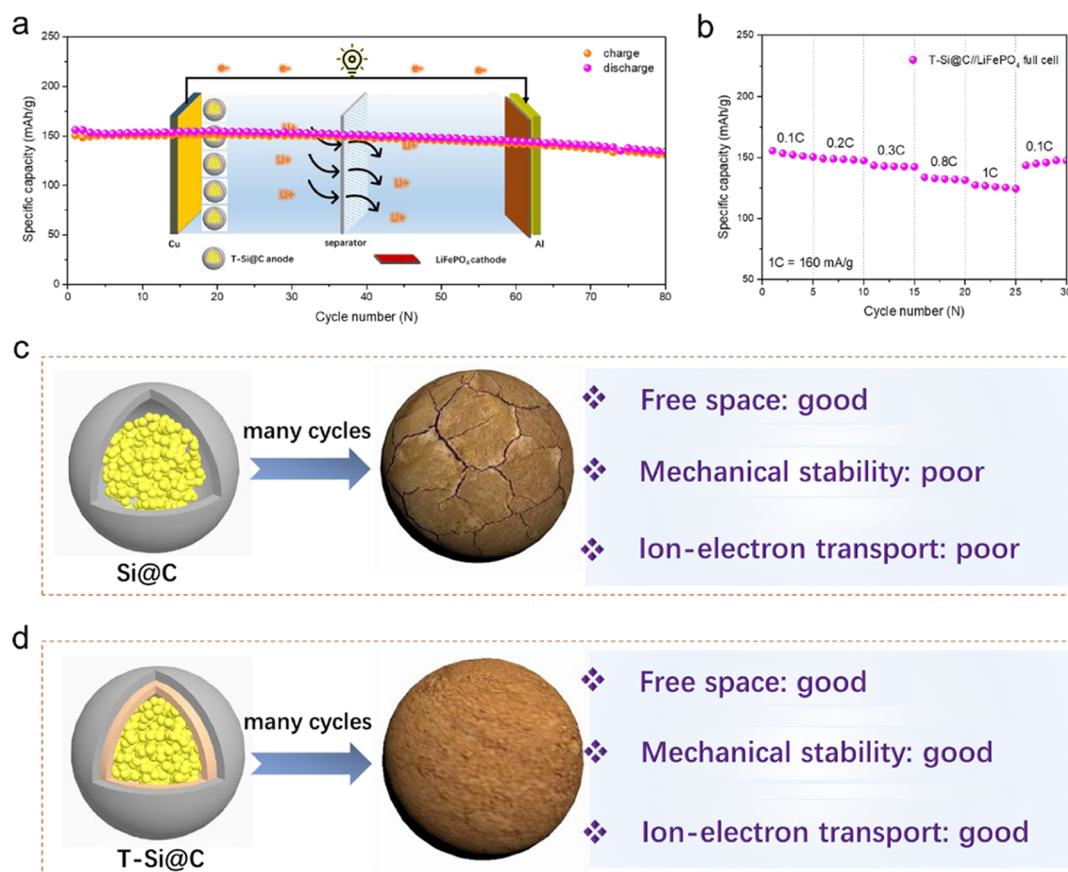
Figure 5. Electrochemical performance of T-Si@C//LiFePO$_4$ full cells: (a) cycling stability at 0.2C; (b) rate capability. Diagram of the structural evolution during cycling and the corresponding advantages and drawbacks: (c) Si@C and (d) T-Si@C.

that of the T-Si@C electrode, indicating a relatively low lithium-ion diffusion after 100 cycles.

To confirm the structural stability of the heterogeneous shell, TEM was performed on the T-Si@C and Si@C anodes after 100 cycles. In Figure 4e, the carbon shell of the Si@C anode shows some cracks due to volume expansion. A broken shell will induce interfacial reactions leading to capacity loss and low Coulombic efficiencies, which is confirmed by the results shown in Figure 3e. In contrast, the T-Si@C anode maintains its structural integrity due to the grid of TiO$_2$/Ti$_5$Si$_3$ nanoparticles on the shell as shown in Figure 4f. In comparison, the nano-Si electrode shows intensive cracking on the surface (Figure 4g). The T-Si@C and Si@C electrodes before cycling are shown in Figure S17. Figure 4h,i show the Si@C and T-Si@C electrodes after cycling, respectively. The relatively intact structure and lack of cracks indicate that free space plays an important role in the structural stability of the electrode. The magnified image in the inset shows that T-Si@C has a smoother surface than Si@C due to better interfacial stability. The SEI of Si@C will be continuously generated as the surface is damaged, resulting in a rough surface. It has therefore been shown that the multiple buffering mechanisms including free space and a hybrid shell configuration play a vital role in maintaining the structural integrity of silicon anodes and thus help to ensure a long cycle-life span.

To assess the practicality of T-Si@C anodes, a T-Si@C// LiFePO$_4$ full cell was constructed using a precycled T-Si@C electrode with available Coulombic efficiencies. A schematic diagram of the full cell is shown in the inset of Figure 5a. The

commercial LiFePO$_4$ cathodes in half cells were tested, and they show excellent electrochemical performance as shown in Figure S18, including good cycling stability and outstanding rate performance. The initial five charge−discharge curves after battery formation are shown in Figure S19, and the average voltage is 2.98 V. Based on the total mass of the anode and cathode, the energy density of the full cell can reach up to 400 Wh kg^{-1}. This full cell exhibits good cycling reversibility with a capacity retention of 87% after 80 cycles. Additionally, good rate capability was displayed with a capacity of 125 mA h g^{-1} at 1C. The promising electrochemical performance of the T-Si@ C//LiFePO$_4$ full cell indicates the feasibility of T-Si@C anodes for practical applications.

Based on this analysis, the impressive lithium storage performance of T-Si@C is due to the multiple volume buffering mechanisms, including free space and a heterogeneous carbon-TiO$_2$/Ti$_5$Si$_3$ shell. Specifically, (1) the free space accommodates the swelling/shrinking of silicon to a large extent, maintaining the structural integrity of the T-Si@C electrode; (2) the heterogeneous configuration of the carbon skin with rigid TiO$_2$/Ti$_5$Si$_3$ nanoparticles further mitigates the stress caused by volume change, and the heterogeneous configuration greatly enhances the mechanical strength of the shell; (3) besides, the hybrid shell provides the reasonably configured ion-electron transport and accelerates lithium-ion diffusion dynamics, which boosts the electrochemical reaction rate. For T-Si@C and Si@C, a schematic diagram of the structural evolution during cycling and the corresponding advantages and drawbacks are shown in Figure 5c,d.

3. CONCLUSIONS

In summary, we demonstrated a silicon-based composite with multiple volume buffering mechanisms by integrating free space and heterogeneous shells composed of carbon and TiO_2/Ti_5Si_3 to improve the ion-electron transport and mechanical stability. In this configuration, the free space and the heterogeneous shell with amorphous carbon and rigid TiO_2/Ti_5Si_3 nanoparticles improve the structural stability. Simultaneously, the hybrid interlayer also considers the rational configuration of ion-electron transport kinetics. Accordingly, T-Si@C anodes combine the outstanding lithium storage performance with excellent long-term cycling stability (876 mA h g^{-1} after 2800 cycles) and impressive rate capability. A T-Si@C//LiFePO$_4$ full cell with an energy density of 400 Wh kg^{-1} also displays good cycling stability and rate performance. This work affords fresh insight into the rational structural manipulation of silicon anodes for long cycle-life electrochemical applications.

■ ASSOCIATED CONTENT

Ⓢ Supporting Information

The Supporting Information is available free of charge at https://pubs.acs.org/doi/10.1021/acsami.0c21455.

> Experimental details; a digital photograph of steel reactor; additional physical and electrochemical characterizations containing the XRD patterns of the SiO$_2$@C and SiO$_2$@TiO$_2$@C, TG curves of SiO$_2$@C and SiO$_2$@TiO$_2$@C, SEM images of SiO$_2$ spheres and SiO$_2$@C; SEM images of SiO$_2$@TiO$_2$ and SiO$_2$@TiO$_2$@C; SEM images of the Si@C and T-Si@C electrodes; a line scan and point EDS of T-Si@C; the charge−discharge curves of Si@C anode and nano-Si anode; CV curves of Si@C; rate and cycling performance of nano-Si anode; EIS spectra of nano-Si electrode; the electrochemical performance of LiFePO$_4$ in half cells; charge−discharge curves of the full cell (PDF)

■ AUTHOR INFORMATION

Corresponding Authors

Pengjian Zuo − *MIIT Key Laboratory of Critical Materials Technology for New Energy Conversion and Storage, School of Chemistry and Chemical Engineering, Harbin Institute of Technology, Harbin 150001, China;* ⓘ orcid.org/0000-0001-8777-5105; Email: zuopj@hit.edu.cn

Geping Yin − *MIIT Key Laboratory of Critical Materials Technology for New Energy Conversion and Storage, School of Chemistry and Chemical Engineering, Harbin Institute of Technology, Harbin 150001, China;* ⓘ orcid.org/0000-0002-8804-6550; Email: yingeping@hit.edu.cn

Xueliang Sun − *Department of Mechanical and Materials Engineering, University of Western Ontario, London, Ontario N6A 5B9, Canada;* ⓘ orcid.org/0000-0003-0374-1245; Email: xsun9@uwo.ca

Authors

Tiansheng Mu − *MIIT Key Laboratory of Critical Materials Technology for New Energy Conversion and Storage, School of Chemistry and Chemical Engineering, Harbin Institute of Technology, Harbin 150001, China; Department of Mechanical and Materials Engineering, University of Western Ontario, London, Ontario N6A 5B9, Canada*

Shuaifeng Lou − *MIIT Key Laboratory of Critical Materials Technology for New Energy Conversion and Storage, School of Chemistry and Chemical Engineering, Harbin Institute of Technology, Harbin 150001, China;* ⓘ orcid.org/0000-0002-1800-9105

Nathaniel Graham Holmes − *Department of Mechanical and Materials Engineering, University of Western Ontario, London, Ontario N6A 5B9, Canada*

Changhong Wang − *Department of Mechanical and Materials Engineering, University of Western Ontario, London, Ontario N6A 5B9, Canada*

Mengxue He − *MIIT Key Laboratory of Critical Materials Technology for New Energy Conversion and Storage, School of Chemistry and Chemical Engineering, Harbin Institute of Technology, Harbin 150001, China; Department of Mechanical and Materials Engineering, University of Western Ontario, London, Ontario N6A 5B9, Canada*

Baicheng Shen − *MIIT Key Laboratory of Critical Materials Technology for New Energy Conversion and Storage, School of Chemistry and Chemical Engineering, Harbin Institute of Technology, Harbin 150001, China*

Xiaoting Lin − *Department of Mechanical and Materials Engineering, University of Western Ontario, London, Ontario N6A 5B9, Canada*

Yulin Ma − *MIIT Key Laboratory of Critical Materials Technology for New Energy Conversion and Storage, School of Chemistry and Chemical Engineering, Harbin Institute of Technology, Harbin 150001, China*

Ruying Li − *Department of Mechanical and Materials Engineering, University of Western Ontario, London, Ontario N6A 5B9, Canada*

Chunyu Du − *MIIT Key Laboratory of Critical Materials Technology for New Energy Conversion and Storage, School of Chemistry and Chemical Engineering, Harbin Institute of Technology, Harbin 150001, China;* ⓘ orcid.org/0000-0003-0547-7724

Jiajun Wang − *MIIT Key Laboratory of Critical Materials Technology for New Energy Conversion and Storage, School of Chemistry and Chemical Engineering, Harbin Institute of Technology, Harbin 150001, China;* ⓘ orcid.org/0000-0002-3643-157X

Complete contact information is available at:
https://pubs.acs.org/10.1021/acsami.0c21455

Author Contributions

T.M.: Designed and performed this experiment and drafted the manuscript. S.L. and N.G.H.: Polished this manuscript. C.W., M.H., B.S.: Performed XRD, TEM, and SEM tests. X.L., Y.M., R.L.: Helped debug the test equipment. C.D., J.W.: Proposed some modifications for this manuscript. P.Z., G.Y., and X.S.: Guided the whole experiment and manuscript writing.

Notes

The authors declare no competing financial interest.

■ ACKNOWLEDGMENTS

■ REFERENCES

(1) Wu, H.; Chan, G.; Choi, J. W.; Ryu, I.; Yao, Y.; McDowell, M. T.; Lee, S. W.; Jackson, A.; Yang, Y.; Hu, L.; Cui, Y. Stable cycling of double-walled silicon nanotube battery anodes through solid-electrolyte interphase control. *Nat. Nanotechnol.* **2012**, *7*, 310−315.

(2) Liu, K.; Liu, Y.; Zhu, H.; Dong, X.; Wang, Y.; Wang, C.; Xia, Y. NaTiSi2O6/C Composite as a Novel Anode Material for Lithium-Ion Batteries. *Acta Phys.-Chim. Sin.* **2020**, *36*, No. 1912030.

(3) Zhu, B.; Wang, X.; Yao, P.; Li, J.; Zhu, J. Towards high energy density lithium battery anodes: silicon and lithium. *Chem. Sci.* **2019**, *10*, 7132−7148.

(4) Pu, K.-C.; Zhang, X.; Qu, X.-L.; Hu, J.-J.; Li, H.-W.; Gao, M.-X.; Pan, H.-G.; Liu, Y.-F. Recently developed strategies to restrain dendrite growth of Li metal anodes for rechargeable batteries. *Rare Met.* **2020**, *39*, 616−635.

(5) Yang, J.; Wang, Y.; Li, W.; Wang, L.; Fan, Y.; Jiang, W.; Luo, W.; Wang, Y.; Kong, B.; Selomulya, C.; Liu, H. K.; Dou, S. X.; Zhao, D. Amorphous TiO2 Shells: A Vital Elastic Buffering Layer on Silicon Nanoparticles for High-Performance and Safe Lithium Storage. *Adv. Mater.* **2017**, *29*, No. 1700523.

(6) Kovalenko, I.; Zdyrko, B.; Magasinski, A.; Hertzberg, B.; Milicev, Z.; Burtovyy, R.; Luzinov, I.; Yushin, G. A. major Constituent of Brown Algae for Use in High-Capacity Li-Ion Batteries. *Science* **2011**, *334*, 75−79.

(7) Kwon, T.-w.; Choi, J. W.; Coskun, A. Prospect for Supramolecular Chemistry in High-Energy-Density Rechargeable Batteries. *Joule* **2019**, *3*, 662−682.

(8) Shin, J.; Kim, T.-H.; Lee, Y.; Cho, E. Key functional groups defining the formation of Si anode solid-electrolyte interphase towards high energy density Li-ion batteries. *Energy Storage Mater.* **2020**, *25*, 764−781.

(9) Wu, S.-J.; Wu, Z.-H.; Fang, S.; Qi, X.-P.; Yu, B.; Yang, J.-Y. A comparison of core−shell Si/C and embedded structure Si/C composites as negative materials for lithium-ion batteries. *Rare Met.* **2019**, 1−7.

(10) Liu, N.; Lu, Z.; Zhao, J.; McDowell, M. T.; Lee, H. W.; Zhao, W.; Cui, Y. A pomegranate-inspired nanoscale design for large-volume-change lithium battery anodes. *Nat. Nanotechnol.* **2014**, *9*, 187−192.

(11) Yoo, J. K.; Kim, J.; Jung, Y. S.; Kang, K. Scalable fabrication of silicon nanotubes and their application to energy storage. *Adv. Mater.* **2012**, *24*, 5452−5456.

(12) Wang, B.; Li, X.; Luo, B.; Hao, L.; Zhou, M.; Zhang, X.; Fan, Z.; Zhi, L. Approaching the downsizing limit of silicon for surface-controlled lithium storage. *Adv. Mater.* **2015**, *27*, 1526−1532.

(13) Chen, B.; Zu, L.; Liu, Y.; Meng, R.; Feng, Y.; Peng, C.; Zhu, F.; Hao, T.; Ru, J.; Wang, Y.; Yang, J. Space-Confined Atomic Clusters Catalyze Superassembly of Silicon Nanodots within Carbon Frameworks for Use in Lithium-Ion Batteries. *Angew. Chem., Int. Ed.* **2020**, *59*, 3137−3142.

(14) Zhang, L.; Rajagopalan, R.; Guo, H.; Hu, X.; Dou, S.; Liu, H. A Green and Facile Way to Prepare Granadilla-Like Silicon-Based Anode Materials for Li-Ion Batteries. *Adv. Funct. Mater.* **2016**, *26*, 440−446.

(15) Philippe, B.; Dedryvere, R.; Gorgoi, M.; Rensmo, H.; Gonbeau, D.; Edstrom, K. Improved performances of nanosilicon electrodes using the salt LiFSI: a photoelectron spectroscopy study. *J. Am. Chem. Soc.* **2013**, *135*, 9829−9842.

(16) Chen, J.; Fan, X.; Li, Q.; Yang, H.; Khoshi, M. R.; Xu, Y.; Hwang, S.; Chen, L.; Ji, X.; Yang, C.; He, H.; Wang, C.; Garfunkel, E.; Su, D.; Borodin, O.; Wang, C. Electrolyte design for LiF-rich solid−electrolyte interfaces to enable high-performance microsized alloy anodes for batteries. *Nat. Energy* **2020**, *5*, 386−397.

(17) Jin, Y.; Kneusels, N. H.; Marbella, L. E.; Castillo-Martinez, E.; Magusin, P.; Weatherup, R. S.; Jonsson, E.; Liu, T.; Paul, S.; Grey, C. P. Understanding Fluoroethylene Carbonate and Vinylene Carbonate Based Electrolytes for Si Anodes in Lithium Ion Batteries with NMR Spectroscopy. *J. Am. Chem. Soc.* **2018**, *140*, 9854−9867.

(18) Xu, Z.; Yang, J.; Zhang, T.; Nuli, Y.; Wang, J.; Hirano, S.-I. Silicon Microparticle Anodes with Self-Healing Multiple Network Binder. *Joule* **2018**, *2*, 950−961.

(19) Wu, Z.-L.; Ji, S.-B.; Liu, L.-K.; Xie, T.; Tan, L.; Tang, H.; Sun, R.-G. High-performance SiO/C as anode materials for lithium-ion batteries using commercial SiO and glucose as raw materials. *Rare Met.* **2020**, DOI: 10.1007/s12598-020-01445-x.

(20) Song, M.-S.; Chang, G.; Jung, D.-W.; Kwon, M.-S.; Li, P.; Ku, J.-H.; Choi, J.-M.; Zhang, K.; Yi, G.-R.; Cui, Y.; Park, J. H. Strategy for Boosting Li-Ion Current in Silicon Nanoparticles. *ACS Energy Lett.* **2018**, *3*, 2252−2258.

(21) Stram, L.; Miroshnikov, Y.; Zitoun, D. Lithiation Kinetics in Silicon/Mn3O4 Core−Shell Nanoparticles Anodes for Li-Ion Battery. *Chem. Mater.* **2019**, *31*, 8320−8327.

(22) Yang, J.; Wang, Y.; Li, W.; Wang, L.; Fan, Y.; Jiang, W.; Luo, W.; Wang, Y.; Kong, B.; Selomulya, C.; Liu, H. K.; Dou, S. X.; Zhao, D. Amorphous TiO2 Shells: A Vital Elastic Buffering Layer on Silicon Nanoparticles for High-Performance and Safe Lithium Storage. *Adv. Mater.* **2017**, No. 1700523.

(23) Jin, Y.; Li, S.; Kushima, A.; Zheng, X.; Sun, Y.; Xie, J.; Sun, J.; Xue, W.; Zhou, G.; Wu, J.; Shi, F.; Zhang, R.; Zhu, Z.; So, K.; Cui, Y.; Li, J. Self-healing SEI enables full-cell cycling of a silicon-majority anode with a coulombic efficiency exceeding 99.9%. *Energy Environ. Sci.* **2017**, *10*, 580−592.

(24) He, Y.; Yu, X.; Wang, Y.; Li, H.; Huang, X. Alumina-coated patterned amorphous silicon as the anode for a lithium-ion battery with high coulombic efficiency. *Adv. Mater.* **2011**, *23*, 4938−4941.

(25) Zhu, B.; Liu, N.; McDowell, M.; Jin, Y.; Cui, Y.; Zhu, J. Interfacial stabilizing effect of ZnO on Si anodes for lithium ion battery. *Nano Energy* **2015**, *13*, 620−625.

(26) Yi, T.-F.; Mei, J.; Peng, P.-P.; Luo, S. Facile synthesis of polypyrrole-modified Li5Cr7Ti6O25 with improved rate performance as negative electrode material for Li-ion batteries. *Composites, Part B* **2019**, *167*, 566−572.

(27) Lopez, J.; Mackanic, D. G.; Cui, Y.; Bao, Z. Designing polymers for advanced battery chemistries. *Nat. Rev. Mater.* **2019**, *4*, 312−330.

(28) Zhang, L.; Wang, C.; Dou, Y.; Cheng, N.; Cui, D.; Du, Y.; Liu, P.; Al-Mamun, M.; Zhang, S.; Zhao, H. A unique yolk-shell structured silicon anode with superior conductivity and high tap density for full Li-ion batteries. *Angew. Chem., Int. Ed.* **2019**, *58*, 8824−8828.

(29) Wang, F.; Wang, B.; Ruan, T.; Gao, T.; Song, R.; Jin, F.; Zhou, Y.; Wang, D.; Liu, H.; Dou, S. Construction of Structure-Tunable Si@Void@C Anode Materials for Lithium-Ion Batteries through Controlling the Growth Kinetics of Resin. *ACS Nano* **2019**, *13*, 12219−12229.

(30) Fang, S.; Shen, L.; Xu, G.; Nie, P.; Wang, J.; Dou, H.; Zhang, X. Rational design of void-involved Si@TiO2 nanospheres as high-performance anode material for lithium-ion batteries. *ACS Appl. Mater. Interfaces* **2014**, *6*, 6497−6503.

(31) Choi, K.; Choi, H.; Sohn, I. Understanding the Magnesiothermic Reduction Mechanism of TiO2 to Produce Ti. *Metall. Mater. Trans. B* **2017**, *48*, 922−932.

(32) Xiao, Q.; Gu, M.; Yang, H.; Li, B.; Zhang, C.; Liu, Y.; Liu, F.; Dai, F.; Yang, L.; Liu, Z.; Xiao, X.; Liu, G.; Zhao, P.; Zhang, S.; Wang, C.; Lu, Y.; Cai, M. Inward lithium-ion breathing of hierarchically porous silicon anodes. *Nat. Commun.* **2015**, *6*, No. 8844.

(33) Yang, D.; Qiu, F.; Zhao, Q.; Wang, L.; Jiang, Q. The abrasive wear behavior of Al2014 composites reinforced with Ti 5 Si 3 -coated SiC P. *Tribol. Int.* **2017**, *112*, 33−41.

(34) Zhou, Z.; Dong, P.; Wang, D.; Liu, M.; Duan, J.; Nayaka, G. P.; Wang, D.; Xu, C.; Hua, Y.; Zhang, Y. Silicon-titanium nanocomposite synthesized via the direct electrolysis of SiO2/TiO2 precursor in molten salt and their performance as the anode material for lithium ion batteries. *J. Alloys Compd.* **2019**, *781*, 362−370.

(35) Luo, W.; Wang, Y.; Wang, L.; Jiang, W.; Chou, S.-L.; Dou, S. X.; Liu, H. K.; Yang, J. Silicon/Mesoporous Carbon/Crystalline TiO2 Nanoparticles for Highly Stable Lithium Storage. *ACS Nano* **2016**, *10*, 10524−10532.

(36) An, H.; Jiang, L.; Li, F.; Wu, P.; Zhu, X.; Wei, S.; Zhou, Y. Hydrogel-Derived Three-Dimensional Porous Si-CNT@G Nanocomposite with High-Performance Lithium Storage. *Acta Phys.-Chim. Sin.* **2020**, *36*, No. 1905034.

(37) Mao, W.; Bao, K.; Cao, F.; Ye, L.; Xie, H.; Li, B.; Wang, W. Facile and scalable synthesis of Ti5Si3 nanoparticles via solid-state route in an autoclave. *J. Superhard Mater.* **2017**, *39*, 117−121.

(38) Zhong, Y.; Yue, C.; Chen, B.; Sun, S.; Zheng, M.; Zhao, L.; Wu, S.; Li, J.; Kang, J.; Lin, L. Synthetic preparation of novel 3D Si/TiO2−Ti2O3composite nanorod arrays as anodes in lithium ion batteries. *RSC Adv.* **2015**, *5*, 37399−37404.

(39) Entwistle, J.; Rennie, A.; Patwardhan, S. A review of magnesiothermic reduction of silica to porous silicon for lithium-ion battery applications and beyond. *J. Mater. Chem. A* **2018**, *6*, 18344−18356.

(40) Yan, Z.; Guo, J. High-performance silicon-carbon anode material via aerosol spray drying and magnesiothermic reduction. *Nano Energy* **2019**, *63*, No. 103845.

(41) Ma, Y.; Desta Asfaw, H.; Liu, C.; Wei, B.; Edström, K. Encasing Si particles within a versatile TiO $2−x$ F x layer as an extremely reversible anode for high energy-density lithium-ion battery. *Nano Energy* **2016**, *30*, 745−755.

(42) Kim, D. W.; Park, A. R.; Oh, T. S.; Lee, N. E.; Yoo, P. J.; Yoo, J. B. Porous MoS2@C heteroshell with a Si yolk structure with improved lithium transport properties and superior cycle stability. *J. Mater. Chem. A* **2017**, *5*, 14906−14913.

(43) Guo, F.; Chen, P.; Kang, T.; Wang, Y.; Liu, C.; Shen, Y.; Lu, W.; Chen, L. Silicon-loaded Lithium-Carbon Composite Microspheres as Lithium Secondary Battery Anodes. *Acta Phys.-Chim. Sin.* **2019**, *35*, 1365−1371.

(44) Xu, Q.; Sun, J. K.; Yu, Z. L.; Yin, Y. X.; Xin, S.; Yu, S. H.; Guo, Y. G. SiOx Encapsulated in Graphene Bubble Film: An Ultrastable Li-Ion Battery Anode. *Adv. Mater.* **2018**, *30*, No. 1707430.

(45) Jang, J.; Kang, I.; Choi, J.; Jeong, H.; Yi, K. W.; Hong, J.; Lee, M. Molecularly Tailored Lithium-Arene Complex Enables Chemical Prelithiation of High-Capacity Lithium-Ion Battery Anodes. *Angew. Chem., Int. Ed.* **2020**, *59*, 2−10.

(46) Ryu, J.; Hong, D.; Choi, S.; Park, S. Synthesis of Ultrathin Si Nanosheets from Natural Clays for Lithium-Ion Battery Anodes. *ACS Nano* **2016**, *10*, 2843−2851.

(47) Pan, Q.; Zuo, P.; Mu, T.; Du, C.; Cheng, X.; Ma, Y.; Gao, Y.; Yin, G. Improved electrochemical performance of micro-sized SiO-based composite anode by prelithiation of stabilized lithium metal powder. *J. Power Sources* **2017**, *347*, 170−177.

(48) Xiu, Z.; Alfaruqi, M. H.; Gim, J.; Song, J.; Kim, S.; Duong, P. T.; Baboo, J. P.; Mathew, V.; Kim, J. MOF-derived mesoporous anatase TiO2 as anode material for lithium−ion batteries with high rate capability and long cycle stability. *J. Alloys Compd.* **2016**, *674*, 174−178.

(49) Wu, J.; Liu, J.; Wang, Z.; Gong, X.; Wang, Y. A new design for Si wears double jackets used as a high-performance lithium-ion battery anode. *Chem. Eng. J.* **2019**, *370*, 565−572.

(50) Li, J.; Li, Z.; Huang, W.; Chen, L.; Lv, F.; Zou, M.; Qian, F.; Huang, Z.; Lu, J.; Li, Y. A Facile Strategy to Construct Silver-Modified, ZnO-Incorporated and Carbon-Coated Silicon/Porous-Carbon Nanofibers with Enhanced Lithium Storage. *Small* **2019**, *15*, No. 1900436.

(51) Liang, J.; Li, X.; Zhu, Y.; Guo, C.; Qian, Y. Hydrothermal synthesis of nano-silicon from a silica sol and its use in lithium ion batteries. *Nano Res.* **2015**, *8*, 1497−1504.

(52) Kwon, H. J.; Hwang, J. Y.; Shin, H. J.; Jeong, M. G.; Chung, K. Y.; Sun, Y. K.; Jung, H. G. Nano/Microstructured Silicon-Carbon Hybrid Composite Particles Fabricated with Corn Starch Biowaste as Anode Materials for Li-Ion Batteries. *Nano Lett.* **2020**, *20*, 625−635.

(53) Shao, R.; Niu, J.; Zhu, F.; Dou, M.; Zhang, Z.; Wang, F. A facile and versatile strategy towards high-performance Si anodes for Li-ion capacitors: Concomitant conductive network construction and dual-interfacial engineering. *Nano Energy* **2019**, *63*, No. 103824.